2005-06-01

Differentiation between melt and freeze stages of the melt cycle using SSM/I channel ratios

David G. Long
david_long@byu.edu

Ivan S. Ashcraft

Original Publication Citation

Ashcraft, I. S., and D. G. Long. "Differentiation between Melt and Freeze Stages of the Melt Cycle using SSM/I Channel Ratios." Geoscience and Remote Sensing, IEEE Transactions on 43.6 (25): 1317-23

Differentiation Between Melt and Freeze Stages of the Melt Cycle Using SSM/I Channel Ratios

Ivan S. Ashcraft, *Member, IEEE,* and David G. Long, *Senior Member, IEEE*

***Abstract*—Microwave remote sensing detection of snow melt and ablation generally focuses on the detection of liquid moisture in the snow-pack. For ablation estimation, it is important to determine if wet snow is in the process of melting or freezing. The different stages of the melt cycle are observed in the diurnal variation of T_b measurements from the Special Sensor Microwave Imager (SSM/I) over Greenland. SSM/I channel ratios exhibit patterns indicating that they are sensitive to melt and freeze stages of the daily melt cycle. The horizontal to vertical polarization ratio is sensitive to surface wetness associated with melting. The 19–37-GHz frequency ratio is sensitive to a frozen surface layer over wet snow which is associated with the freeze stage of the melt cycle. These observations are supported by conceptual models presented here and in *in situ* measurements from other investigators.**

***Index Terms*—Brightness temperature, freeze/thaw, Greenland, melt detection, Special Sensor Microwave Imager (SSM/I).**

I. Introduction

MASS balance of the Greenland ice sheet is a key factor in global sea level change [1], [2]. The harsh environment in Greenland combined with the immense size of the ice-sheet makes it difficult to collect sufficient *in situ* data to monitor the effects of global climate change on Greenland mass balance. Remote sensing is a practical alternative for studying the ice sheet. Microwave datasets from spaceborne instruments have many favorable attributes including regular frequent coverage of the entire ice sheet and high sensitivity to melt. Estimation of the duration and extent of the annual melt is important in estimating ablation, a critical piece of the overall mass balance.

Various methods have been developed for detection of melt over Greenland snow using microwave measurements. Previous studies have demonstrated microwave sensors' ability to detect the extent and duration of melt across the ice sheet [2]–[7]. The methods generally focus on detecting the presence of liquid water in the snow. However, a snow-surface containing liquid water can be in one of two states: melting or freezing. When the amount of liquid water in the snow-pack is increasing over time, the net heat flow is into the snow, and the snow is in the melt state. If the liquid water is decreasing, the net heat flow is out of the wet snow so the snow is classified as freezing. In this generalization, changes in the liquid water content due to percolation are ignored for simplification. The distinction between the melt and freeze stages of the melt cycle is important because ablation occurs when heat is flowing into the snow causing liquid water to form. Minimal ablation is expected during periods when heat is flowing out from the surface and liquid water is transforming back to its frozen state.

Increased accuracy in ablation estimation requires differentiation between the melt and freeze stages of the melt cycle. This differentiation is possible based on fundamental differences due to frequency and polarization in the sensitivity of T_b to snow melt and refreeze. These differences are observed using SSM/I channel ratios. The relationship between the channel ratios and the melt cycle stages are established through empirical observations and supported by basic microwave emission modeling. The results in this paper lay a framework for the discrimination between the melt and freeze stages of the melt cycle.

This paper is organized as follows. First, a background discussion on the dataset and the data processing method is presented. Then, diurnal signatures of T_b are analyzed and compared with automatic weather station temperature measurements. Next, diurnal variations in SSM/I channel ratios are related to the stages of melt, which is supported by *in situ* data from other investigators. Finally, theory supporting this method for melt classification is presented.

II. Data

This study employs data from the Special Sensor Microwave Imager (SSM/I) instrument, a bipolar multifrequency microwave radiometer which measures T_b using seven channels. The four channels employed in this study include 19- and 37-GHz vertical and horizontal polarizations denoted 19 V, 19 H, 37 V, and 37 H.

The focus of this paper is on the differentiation between the different stages of the melt cycle. Because the surface experiences multiple stages of the melt cycle during one day intervals, the daily average T_b values used in other studies are inadequate in their temporal sampling. In order to achieve increased temporal resolution, we use a nonparametric estimator in conjunction with T_b measurements from multiple instruments.

During the summer of 2002, three SSM/I instruments operated simultaneously aboard the F-13, F-14, and F-15 satellites. Their orbits result in different time-of-day observations for each instrument. Combining measurements from the three instruments provides increased temporal coverage. Based on our analysis, these three sensors appear to be intercalibrated very well, minimizing possible biases in T_b due to calibration differences. The temporal sampling at any location is dependent on the lattitude of the location. The average daily sampling at the various lattitudes for Greenland is illustrated in Fig. 1 using image histograms. These histograms show the density of the

Manuscript received September 7, 2004; revised February 4, 2005.

The authors are with the Center for Remote Sensing, Brigham Young University, Provo, UT 84602 USA (e-mail: long@ee.byu.edu).

Digital Object Identifier 10.1109/TGRS.2005.845642

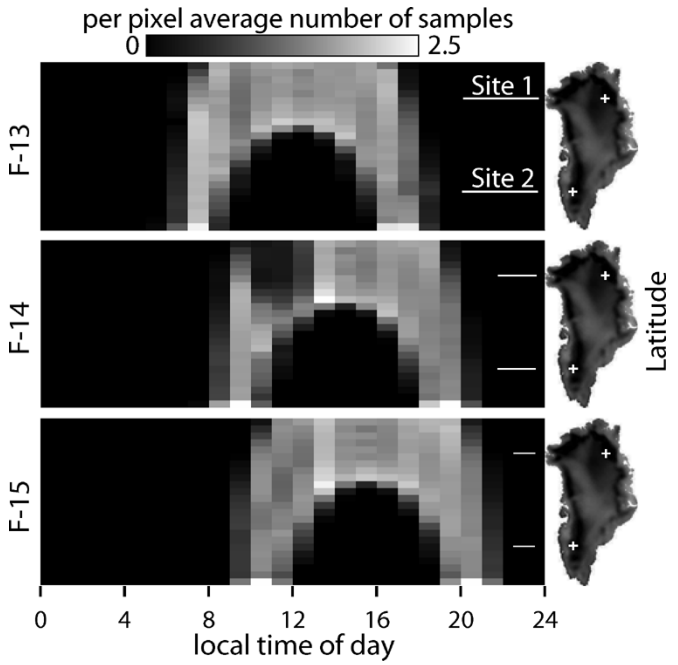

Fig. 1. (Left) Image histograms of the average number of observations versus pass time for pixels at a given latitude for the F-13, F-14, and F-15 satellites versus. Each horizontal scan represents a histogram at the matching latitude on the Greenland image on the right. At high latitudes, the distribution of the temporal sampling is unimodal due to the wide swath orbit inclination angle of the satellites. At lower latitudes, the temporal sampling becomes bimodal with the modes representing ascending and descending passes times. (Right) Brightness temperature images of Greenland indicating the corresponding latitudes on the ice sheet. The images show T_b on JD 15, 2002.

temporal sampling of T_b for the local time of day versus latitude. At high latitudes, each sensor has frequent temporal sampling during an 11-h span of time with a combined span of approximately 14 h of coverage. At lower latitudes, there is a temporal division between ascending and descending measurements. The combined coverage is approximately from 0600–1200 in the morning and 1600–2200 in the evening. Because of relative orbital geometries between the three SSM/I sensors, an 8-h portion (2200-0600) of each day is not observed at any latitude. Note that SSM/I measurements occur primarily during daytime hours which is the period when the highest diurnal temperatures are observed in automatic weather station (AWS) data and the largest amount of melt is expected to occur.

T_b measurements are processed to estimate T_b at regularly spaced increments in space and time. The spatial sampling is 8.9 km, and the temporal sampling is 3 h where T_b is interpolated to obtain estimates at times of day when there are no measurements. For a given location, T_b measurements within a 25- km radius are included in the processing. Estimates of T_b every 3 h are obtained using a simple nonparametric fit to the data where the estimate of T_b at time τ is

$$T_b(\tau) = \frac{\sum_i T_{bi} w(\tau, t_i)}{\sum_i w(\tau, t_i)} \tag{1}$$

where

$$w(\tau, t_i) = e^{-\frac{1}{2}\frac{(t_i-\tau)^2}{\sigma_t^2}} \tag{2}$$

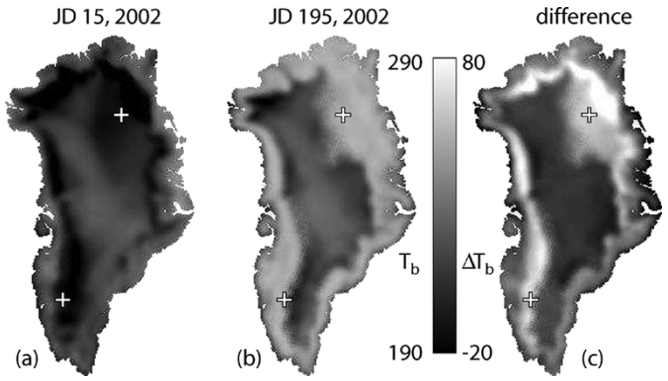

Fig. 2. Greenland SSM/I 19 V T_b images from (a) midwinter (JD 15, 2002) and (b) the peak melt period (JD 195, 2002). The difference is shown in (c). The large differences are primarily caused by the presence of liquid water in the snow from melt. Smaller differences are due to surface temperature change. The Tunu-N site (78.0 N, 34.0 W) is indicated by the upper "+" mark.

is a temporal weighting factor and $\sigma_t = 3$ h, which is the same as the sampling interval. This Gaussian kernel weighs the measurements near the time of interest more heavily than those more distant and enables robust interpolation between data with random spacings ranging from minutes to over 12 h. The sampling frequency of these estimates makes it possible to observe the stages of the daily melt cycle and aids in associating the frequency and polarization sensitivities of T_b with the vertical melt profile.

We consider two study sites. Site one, centered at 78.0 N, 34.0 W (see Fig. 2), is selected for three primary reasons: first, it is the location of the Tunu-N AWS, so air temperature measurements are available. Second, moderate melt is observed in this area during the summer of 2002. Third, nearly continuous temporal coverage exists for T_b (see Fig. 1) and AWS temperature are available over the summer melt time period. Site two, centered at 65.5 N, 47.6 W, is located near the saturation line dividing the percolation and wet snow zones and was arbitrarily selected. Data for this site are studied for 2000.

III. T_b Daily Melt Cycle Observations

The sensitivity of radiometers to snow melt stems from the dramatic effect the presence of liquid water has on the microwave properties of the snow. The Rayleigh–Jeans approximation is

$$T_b = eT \tag{3}$$

where e is the microwave emissivity, and T is the physical temperature of the snow in Kelvin [2]. The emissivity of frozen snow remains relatively constant over time, with small variations due to accumulation and other changes in the geophysical properties of the surface. For a constantant emmissivity T_b is a linear function of T based on the Rayleigh–Jeans approximation. When melt begins, the introduction of liquid water into the snow-pack causes a large increase in e and a corresponding increase in T_b. This is illustrated in the summer T_b image of Fig. 2 where the periphery of the Greenland ice sheet exhibits high T_b values. In this image the melt is particularly strong in northeast Greenland.

Using the high temporal resolution T_b estimates, it is possible to observe changes in T_b related to the stages of the daily

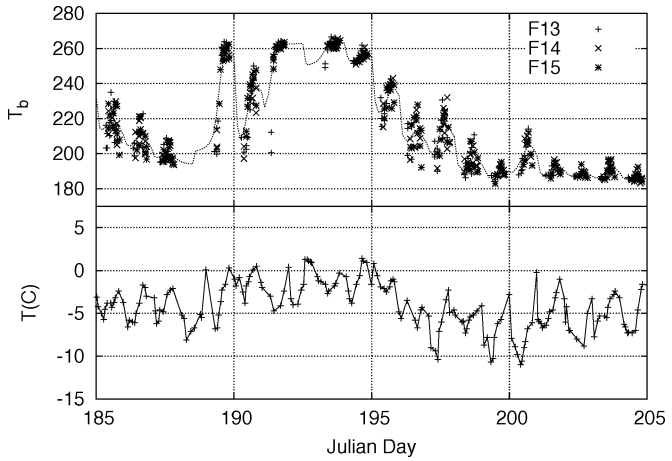

Fig. 3. (Top panel) Raw 19 V T_b measurements from 78.0 N, 34.0 W during the summer of 2002. The line is a nonparametric fit to the raw data with estimates of T_b at 3-h intervals. (Bottom panel) AWS near-surface air temperature measurements at the same location. The horizontal axis is local Greenland time. The vertical spread in the data near the peaks during the period from JD 195 to 200 is attributed to spatial inhomogenities in the refreeze process.

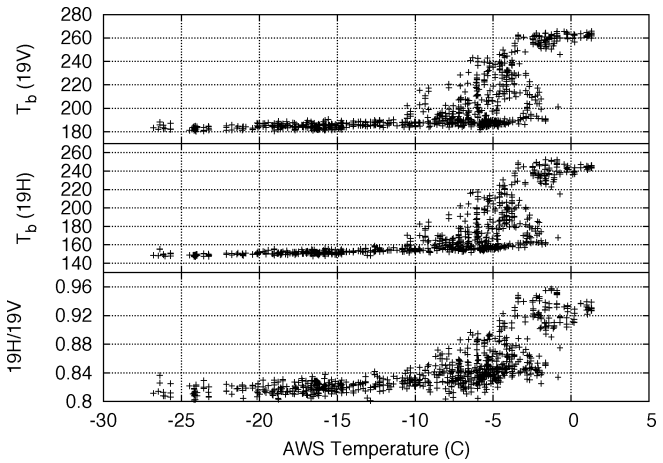

Fig. 4. Scatter plots showing the relationship between $T_{\rm air}$ and 19 V and 19 H T_b values. Data from JD 184 to 236, 2002 are included with measurements from JD 205 to 211 discarded due to the lack of $T_{\rm air}$ measurements during this period. Data are from 78.0 N, 34.0 W.

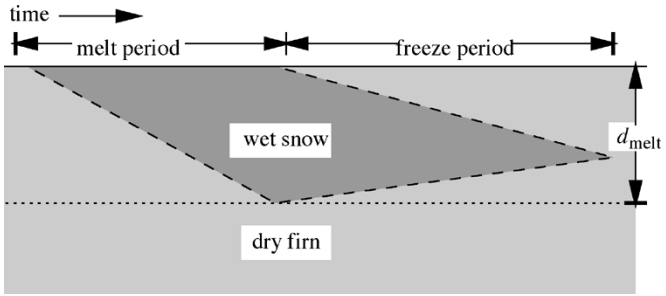

Fig. 5. Illustration of the progression of a simplified vertical melt profile over time.

melt cycle. This is illustrated using T_b estimates centered at the Tunu-N site. An abrupt increase in T_b connected with a melt event is observed in Fig. 3 during the afternoon of JD 189. By early in the morning on JD 190, T_b has dropped significantly due to overnight freezing. By midday on JD 190, the T_b measurements are once again at high values. This pattern of daily melt and nightly freeze is observed each day in the T_b variation. The diurnal variation is due to both temperature cycling and changes in emissivity with the emissivity change dominating during periods of melt/refreeze. This change in emmisivity is due to an increase in the imaginary part of the dielectric constant with the introduction of liquid water into the snowpack dramatically increasing the apsorption coefficient of the snow which is discussed further Section V. T_b measurements between JD 190–195 indicates relatively intense melt. T_b gradually decreases during the period between JD 196 and 200 indicating a gentle refreeze. We attribute the increased spread in the raw data during this period to spatial inhomogeneities in the refreeze process.

AWS near-surface air temperature measurements obtained from the Greenland Climate Network are used to assist in validating melt as the primary contributing factor driving the rapid large fluctuations of the microwave measurements. The AWS temperature data $(T_{\rm air})$ concurs with the microwave dataset in manifesting periods of melt. The days when $T_{\rm air}$ reaches above freezing (JD 190–196) is when the T_b measurements indicate significant melt. After JD 196, $T_{\rm air}$ remains below freezing and the microwave measurements gently migrate to their frozen state.

Fig. 4 illustrates the strong relationship between the microwave measurements and $T_{\rm air}$. The effects of melt are observed in the 19 V and 19 H T_b measurements at $T_{\rm air}$ values as low as -10 °C. Above -2 °C the effects of the melt on T_b saturate at around 260°K for 19 V and 245°K for 19 H. Slight differences in the sensitivity of the 19 V and 19 H channels aid in determining the melt profile. A key difference is illustrated using the 19 H/19 V polarization ratio (see Fig. 4). For $T_{\rm air} < -10$ °C the polarization ratio is ≈0.82. As the temperature increases, the polarization ratio increases to ≈0.94 at $T_{\rm air} = 0$. Further analysis of the 19-GHz polarization ratio is provided in the next section.

Some care is required in interpreting Fig. 4 due to discrepancies expected between $T_{\rm air}$ and the actual surface temperature. Surface temperature change is primarily driven by radiation and conduction whereas convection plays a major role in local air temperature change. This discrepancy is considered to be a contributing factor to the hysteresis effect observed in T_b as a function of $T_{\rm air}$ associated with a melt event. Also, the satellite pass times are during the day when the surface is generally melting, so nighttime trends are not included.

IV. Channel Ratios

An illustration of a simplified vertical melt cycle for this area is shown schematically in Fig. 5. During the melting phase, liquid water forms on the snow grains near the surface, with the depth of the melt increasing over time. During freeze, heat flows both up from the surface and down into the snow-pack. In the case of deep melt, the surface may freeze while liquid water remains in the subsurface snow. Multiple situations with a frozen crust above wet snow were observed by Mätzler [8].

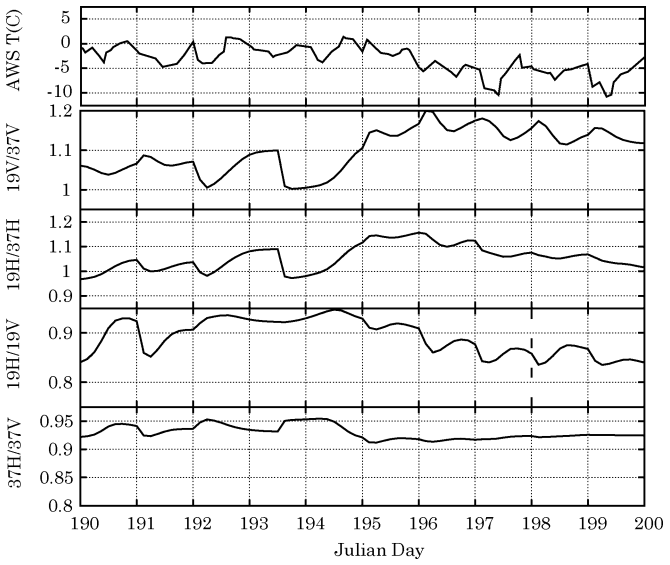

Fig. 6. (Lower panels) Ratios of various nonparametric estimates of SSM/I channel brightness temperatures are valuable in characterizing the melt profile of the surface. Data are for the study location 78.0 N, 34.0 W, 2002. (Upper panel) AWS near-surface air temperature for the same location and time period.

TABLE I
DEFINITIONS FOR THE DIFFERENT SNOW TYPES

snow type	definition
deep dry snow	water equivalent of dry snow is 25 to 63 cm
wet snow	snow surface layer is wet
thin crust	a frozen crust, 1 to 3 cm thick, over wet snow
thick crust	a frozen crust, 4 to 30 cm thick, over wet snow

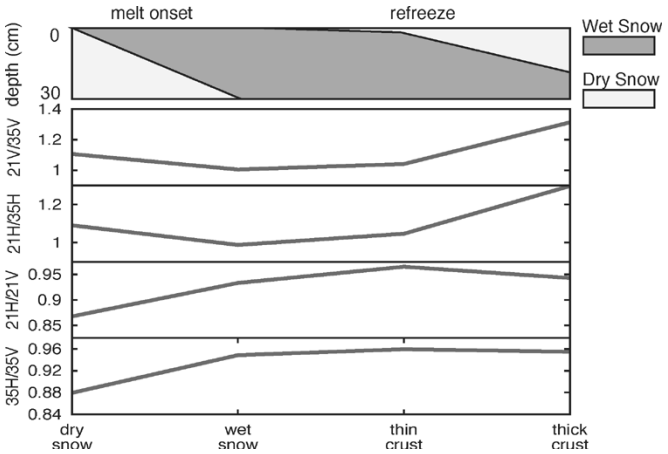

Fig. 7. Channel ratios for certain snow conditions as given by Mätzler [8]. The horizontal axis represents the different snow profiles associated with an idealized melt event. It is in the order of the typical progression of a melt event from dry snow to wet snow to a thin then a thick frozen crust over an underlying layer of wet snow. A simplified illustration of the melt progression is shown above the plots. See Table I for definitions of snow types.

Both surface and subsurface melt contribute to a large effective emissivity resulting in high T_b measurements. However, different polarizations and frequencies respond somewhat differently to the stages of a melt event. Fig. 6 shows various SSM/I channel ratios and the AWS near-surface air temperature. The lower two panels illustrate the polarization dependence while the center panels illustrate the frequency difference. The ratio method has the advantage of minimizing the change in surface temperature and focusing on only differences in emissivity for the two channels.

Variations in the frequency dependence of emissivity aid in detecting periods during which subsurface moisture is present under a frozen surface. The 19 V/37 V and 19 H/37 H plots in Fig. 6 are significantly higher during the period between JD 195 and 200 which is a refreezing period. We attribute this to the difference in the emission depth at the two frequencies. The emission depth at 37 GHz is small, so the frozen surface snow dominates the signal and the measured T_b is small. The emission depth at 19 GHz is larger, so the underlying wet snow has a larger contribution resulting in a larger T_b measurement. During midday when surface melt is most likely, the frequency ratios decrease, migrating closer to one. We attribute this to the small emission depth of wet snow for both frequencies, so both channels are "seeing" only the wet surface layer. Also, the emission depth may be slightly different for the different polarizations as described later in Section III.

In the polarization ratio plots of Fig. 6, maximums occur when surface melt is expected to be present. As discussed in Section III and observed in Fig. 4, h-pol T_b are consistently less than v-pol. During melt, the two emissivities become closer to equal, corresponding to an increase in the polarization ratio. This is observed in the *in situ* data presented later in this section and theoretically explained in Section V. The 19 H/19 V ratio is largest during the period JD 190 to 195 and peaks at midafternoon when surface melting is expected. Minimums occur between late night and early morning during this period when the surface is expected to be freezing due to below freezing air temperatures and radiative cooling. The ratio also decreases during the refreeze period from JD 196 to 200. This occurs because the bulk emission depths are slightly different for horizontal and vertical polarizations as described in Section V.

A. Comparison With In Situ Data

The signatures of different vertical melt profiles observed in the SSM/I channel ratios are compared with *in situ* measurements from Mätzler [8]. Mätzler records T_b values for various frequencies and terrains of which a selected number are similar to Greenland surface profiles. The 21- and 35-GHz frequencies used by Mätzler are the closest to those analyzed herein for SSM/I. The snow conditions observed by Mätzler which are similar to those expected in Greenland are described in Table I.

Fig. 7 shows the polarization and frequency ratios for each of the relevant snow conditions observed by Mätzler (see Table I). The plot is designed so that progression to the right on the horizontal axis corresponds to the progression of an idealized melt event beginning with a layer of dry snow. The snow melts and then the surface begins to refreeze with the frozen crust thickening over time. Consistent with the SSM/I observations, the frequency ratios display a small drop associated with surface melt, progressing toward a large increase affiliated with a thick frozen crust over wet snow. Also similar to SSM/I observations, the polarization ratio increases during a melt event, with a maximum observed during the period when the melt is expected to have maximum depth (a thin frozen crust is present indicating

the transition from melt to freeze). The polarization ratio decreases as the frozen crust thickens.

V. Theory

In order to better understand the physical mechanisms driving the sensitivity of SSM/I channel ratios to the different melt stages, we employ simple electromagnetic models based on the bulk properties of the snow pack. These properties are estimated using various models and observations as discussed below. We first consider the frequency ratio, followed by the polarization ratio.

A. Frequency Ratio

We illustrate the variation in the frequency ratio during the melting and freezing stages of the melt cycle using a simple multilayer model. The brightness temperature at the surface is the sum of the contributions from the individual layers, i.e.,

$$T_b = \sum_{i=1}^{N} T_{bi} \tag{4}$$

where T_{b1} is the contribution from the top layer, T_{b2} is the contribution from the second layer, and T_{bN} is the contribution from the bottom layer. Our model estimates the contribution from the individual layers based on the T_b that would be emitted from a homogeneous infinite halfspace consisting of snow with a uniform temperature profile and physical properties matching the layer of interest. We denote this theoretical brightness temperature as T_b^{∞}. Note that T_b^{∞} can be separated into a contribution from below depth d $(T_b^{\infty} e^{-\kappa_e d \sec\theta})$ and a contribution from above depth d $(T_b^{\infty}(1 - e^{-\kappa_e d \sec\theta}))$ where κ_e is the extinction coefficient of the snow and θ is the propagation angle within the snow. The term $e^{-\kappa_e d \sec\theta}$ represents the extinction of the microwave emission traveling from depth d to the surface. Based on each snow layer representing the top layer of a half space of homogeneous snow, the contribution from layer i is

$$T_{bi} = e^{-\tau_i} T_{bi}^{\infty} (1 - e^{-\kappa_{ei} d_i \sec\theta_i}) \prod_{j=1}^{i} \Upsilon_j \tag{5}$$

where d_i is the depth of the ith layer, θ_i is the propagation angle in the layer, Υ_j is the power transmission at the upper boundary of the jth layer, and $\tau_i = \sum_{j=1}^{i} \kappa_{ej} d_j \sec\theta_j$ is the optical depth of the snow above the ith layer. This model ignores multiple reflections between layers. Due to the small differences in the real part of the dielectric constant between layers (see Table II), the contribution from multiple reflections is assumed to be negligible.

This model is used to simulate the relationship between $T_b(19\text{ V})$ and $T_b(37\text{ V})$ during a melt/freeze cycle. During melt, the vertical profile of the snow is modeled as two layers: wet snow over dry firn, with the depth of the wet snow increasing over time. Dry firn is used rather than new dry snow to simplify the model. Potential discrepancies between the model results and observed data trends due to this simplification are discussed later. During freeze, the surface is modeled as three layers: wet snow between two layers of dry firn. The bottom of the wet snow layer is assumed to freeze at one half the rate of the top of the wet snow layer (see Fig. 5).

TABLE II
Dry and Wet Snow Dielectric Properties Used for the Simple Multilayer Emission Model. The Associated Frequency (f) Is in Gigahertz. All Estimates Are for Vertical Polarization

snow	f	ϵ_r	κ_e	κ_a	κ_s	Υ_{air}	T_b^{∞}
dry	19	1.41	1.58	0.00	1.58	1.00	180
dry	37	1.38	10.20	0.00	10.20	1.00	160
wet	19	1.44 + i0.029	11.32	9.74	1.58	1.00	273
wet	37	1.41 + i0.023	25.18	14.98	10.20	1.00	273

The implementation of this multilayer T_b model requires the estimates of T_b^{∞}, κ_e, and θ for each layer as well as Υ at each layer boundary (see Table II). Our estimates of T_b^{∞} for dry firn are typical of T_b measurements after the summer melt in the southwest percolation zone during the year 2000. Our estimates of T_b^{∞} for wet snow are based on an emissivity $e \approx 1$ and the melting point of ice.

The extinction coefficient (κ_e) of dry snow is estimated using the empirical formula from [9] assuming the snow grain radius to be 0.5 mm. The extinction coefficient of wet snow is estimated using the relationship $\kappa_e = \kappa_s + \kappa_a$ where κ_s is the scattering coefficient and κ_a is the absorption coefficient. The absorption coefficient is a function of the complex relative dielectric constant (ϵ_r), i.e.,

$$\kappa_a = 2\frac{2\pi f}{c} \Im\{\sqrt{\epsilon_r}\} \tag{6}$$

where f is the frequency, c is the speed of light in a vacuum, and $\Im\{\cdot\}$ denotes the imaginary part. The complex relative dielectric constant is estimated using a *modified Debye-like model* from Ulaby *et al.* [10, p. 2072] where the snow is assumed to have a density $\rho = 0.4\ \mathrm{g \cdot cm^3}$. The scattering coefficient for wet snow is assumed to be similar to that of dry snow, which is negligible compared to κ_a of wet snow.

The propagation angle (θ) is calculated using Snell's law with the estimates of ϵ_r. The power transmission (Υ) at the boundaries is calculated from the estimates of ϵ_r using Fresnel reflection. The estimated properties of the dry firn and wet snow are listed in Table II.

Variations in $T_b(19\text{ V})$ and $T_b(37\text{ V})$ during a melt cycle based on this multilayer T_b model are illustrated in Fig. 8. For convenience, we denote T_b^{∞} for the dry firn as T_b^{dry} and T_b^{∞} of the wet snow as T_b^{wet}. During the melt phase, T_b values follow a convex path originating at $T_b^{\mathrm{dry}}(19\text{ V})$, $T_b^{\mathrm{dry}}(37\text{ V})$ and ending at $T_b^{\mathrm{wet}}(19\text{ V})$, $T_b^{\mathrm{wet}}(37\text{ V})$. For shallow melt events, the T_b values follow the same path without reaching the end point. Four different paths are shown for the freeze phase based on different melt depths. Contrary to the melt phase, the path followed by the T_b values during the freeze phase of the melt cycle is significantly affected by the depth of the melt. In all cases, T_b during the freeze phase follows a concave path ending at $T_b^{\mathrm{dry}}(19\text{ V})$, $T_b^{\mathrm{dry}}(37\text{ V})$. The start point lies on the path followed during the melt phase with the location dependent on melt depth. The curvature of the path during the freeze phase increases with the depth of the melt. The results in Fig. 8 confirm the frequency

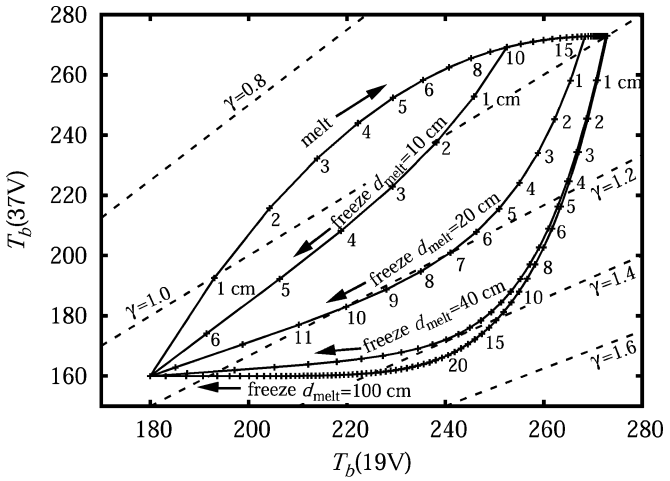

Fig. 8. Simulated melt cycle for $T_b(19\ \mathrm{V})$ and $T_b(37\ \mathrm{V})$ with different melt depths represented. Numbers within the plot indicate incremental melt depths and depths of surface freeze. Lines of constant frequency ratio $(\gamma = T_b(19\ \mathrm{V})/T_b(37\ \mathrm{V}))$ are also shown.

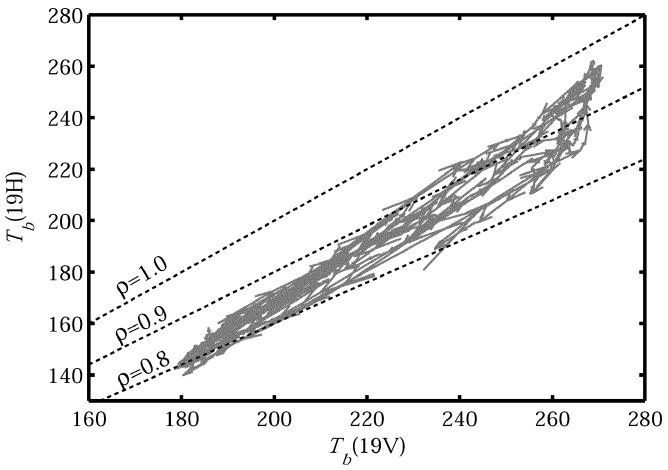

Fig. 10. Plot of $T_b(19\ \mathrm{V})$ versus $T_b(19\ \mathrm{H})$ during the year 2000 at 65.6 N, 47.6 W. The points are connected to indicate the temporal evolution. Lines of constant polarization ratio $(\rho = T_b(19\ \mathrm{H})/T_b(19\ \mathrm{V}))$ are also shown in the plot.

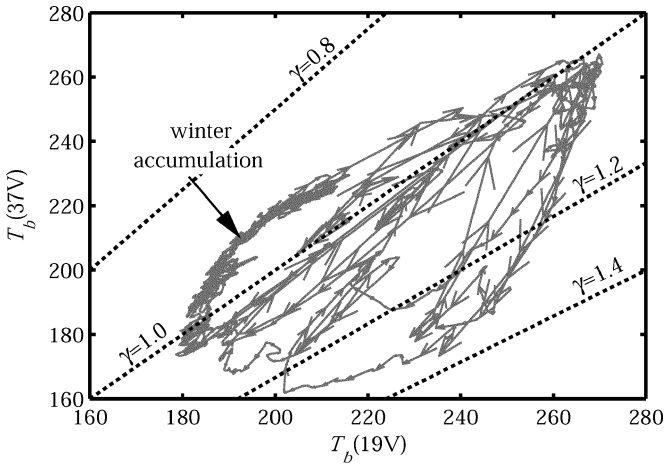

Fig. 9. Plot of $T_b(19\ \mathrm{V})$ versus $T_b(37\ \mathrm{V})$ during the year 2000 at site 2 (65.6 N, 47.6 W). The points are connected to indicate the temporal evolution. The cluster of points near the left side of the plot shows the effects of winter accumulation. Lines of constant frequency ratio (γ) are also shown in the plot.

ratio $\gamma = T_b(19\ \mathrm{V})/T_b(37\ \mathrm{V})$ as a tool for discriminating between the melt and freeze portions of the melt cycle. Additionally, the maximum value of γ during freeze is an indicator of the melt depth.

Fig. 9 shows SSM/I T_b measurements during 2000. These T_b estimates are at 6-h intervals and originate from the SSM/I instrument aboard the F-14 satellite. The points are connected to illustrate the temporal evolution of the measurements. The patterns in Fig. 9 are similar to the simulations shown in Fig. 8. During many of the observed melt cycles, it appears that the surface does not achieve a frozen state before the melting repeats. The melt cycles in the plot show a distinct difference in the melt and refreeze paths, as predicted by the model. The lines of constant frequency ratio (γ) indicate the applicability of this parameter in differentiating between melt and freeze.

The trend in T_b associated with winter accumulation is also indicated in Fig. 9. This migration during the winter is a result of the combination of changes in the surface due to accumulation and temperature variations. The idea of temperature variation alone causing this migration is ruled out based on the premise that temperature changes are expected to result in a straight line migration. Accumulation causes the surface emission to approach the behavior of dry snow which has higher T_b values than the snow in the percolation and wet snow zones. Because of the smaller emission depth, the 37-GHz T_b increases at a faster rate than the 19-GHz T_b.

As mentioned previously, the model ignores the dry snow accumulation on the surface, assuming the snow profile to be comprised of firn prior to the melt event. This effectively ignores the T_b migration observed in Fig. 9 associated with accumulation. This simplification is expected only to affect the start point of the initial melt. After the first melt/freeze cycle, the surface snow is effectively firn.

B. Polarization Ratio

The sensitivity of the polarization ratio to the melt or the freeze stage may be explained based on Fresnel reflection. Assuming that snow layers are isotropic, there is no difference between h-pol and v-pol in propagating through the volume of each snow layer. The polarization is only significant at the layer boundaries. Based on Fresnel reflection, the transmission of v-pol emissions through the boundary is always greater than the transmission of h-pol emissions through the boundary. During melt, the emission depth is small and the observed T_b is primarily from the top snow layer. For a single layer, the ratio of h-pol T_b to v-pol is primarily a function of the reflection at the air/snow interface. During freeze and for dry snow, the emission depth is much greater and many snow layers contribute to the observed T_b. For frozen snow, the ratio of h-pol to v-pol is less, due to additional attenuation of h-pol emissions at subsurface layer interfaces. This effect is illustrated in the SSM/I T_b plot in Fig. 10. In this case, the largest ratio difference is between the end points as opposed to the frequency ratio where the largest difference is in the transition region. The hysteresis effect is smaller than for the frequency ratio, but may still be exploited to infer the melt depth.

VI. Conclusion

Using T_b observations from multiple SSM/Is, which are collected at different local times of day, we have studied the dirunal variability of the T_b measurement. Previous investigators have found T_b to be effective in detecting melt. Here, we have extended this to enable classification of the detected melt within the melt cycle. We find that the T_b polarization ratio and frequency ratio can be used separately or combined to differentiate between the melt onset and the refreeze stages of the melt cycle. The 19–37-GHz frequency ratio increases when the surface is frozen and liquid water is present in the subsurface. The horizontal to vertical polarization ratio increases when liquid water is present in the surface snow. We validate our analysis via simple electromagnetic scattering models and with AWS data. The use of this technique in future studies will enable increased accuracy in ablation estimation and estimation of the overall mass-balance of the Greenland ice-sheet.

References

[1] W. S. B. Paterson and N. Reeh, "Thinning of the ice sheet in northeast Greenland over the past forty years," *Nature*, vol. 414, pp. 60–61, Nov. 2001.

[2] W. Abdalati and K. Steffen, "Snowmelt on the Greenland ice sheet as derived from passive microwave satellite data," *J. Clim.*, vol. 10, pp. 165–175, Feb. 1997.

[3] T. L. Mote and M. R. Anderson, "Variations in snowpack melt on the Greenland ice sheet based on passive-microwave measurements," *J. Glaciol.*, vol. 41, no. 137, pp. 51–60, 1995.

[4] I. S. Ashcraft and D. G. Long, "SeaWinds views Greenland," in *Proc. IGARSS*, vol. 3, 2000, pp. 1131–1136.

[5] V. Wismann, "Monitoring of seasonal snowmelt on Greenland with ERS scatterometer data," *IEEE Trans. Geosci. Remote Sens.*, vol. 38, no. 4, pp. 1821–1826, Jul. 2000.

[6] V. S. Nghiem, K. Steffen, R. Kwak, and W.-Y. Tsai, "Detection of snowmelt regions on the Greenland ice sheet using diurnal backscatter change," *J. Glaciol.*, vol. 47, no. 159, pp. 539–547, 2001.

[7] J. D. Pack and M. A. Jensen, "Greenland snowmelt estimation using multi-spectral passive and active microwave observations," in *Proc. IGARSS*, 2002, pp. 2106–2108.

[8] C. Mätzler, "Passive microwave signatures of landscapes in winter," *Meteorol. Atmos. Phys.*, vol. 54, pp. 241–260, 1994.

[9] M. T. Hallikainen, F. T. Ulaby, and T. E. V. Deventer, "Extinction behavior of dry snow in the 18- to 90-ghz range," *IEEE Trans. Geosci. Remote Sens.*, vol. GE-25, no. 6, pp. 737–745, Nov. 1987.

[10] F. Ulaby, R. Moore, and A. Fung, *Microwave Remote Sensing: Active and Passive*. Norwood, MA: Artech House, 1990, vol. 3.

Ivan S. Ashcraft received the Ph.D. degree in electrical engineering from Brigham Young University (BYU), Provo, UT, in 2004.

At BYU, he worked with the BYU Center for Remote Sensing focusing on applications of microwave remote sensing for monitoring the effects of climate change on the Greenland Ice Sheet. He is currently with BYU, Rexburg, ID.

David G. Long (S'80–SM'98) received the Ph.D. degree in electrical engineering from the University of Southern California, Los Angeles, in 1989.

From 1983 to 1990, he was with the National Aeronautics and Space Administration (NASA) Jet Propulsion Laboratory (JPL), Pasadena, CA, where he developed advanced radar remote sensing systems. While at JPL, he was the Senior Project Engineer on the NASA Scatterometer (NSCAT) project, which was flown aboard the Japanese Advanced Earth Observing System (ADEOS) from 1996 to 1997. He was also the Experiment Manager and Project Engineer for the SCANSCAT scatterometer (now known as SeaWinds). In 1990, he joined the Department of Electrical and Computer Engineering, Brigham Young University (BYU), Provo, UT, where he currently teaches upper division and graduate courses in communications, microwave remote sensing, radar, and signal processing, is the Director of BYU's Center for Remote Sensing, and is the Head of the Microwave Earth Remote Sensing Laboratory. He is the Principal Investigator on several NASA-sponsored interdisciplinary research projects in microwave remote sensing and innovative radar systems. He has numerous publications in signal processing and radar scatterometry. His research interests include microwave remote sensing, radar, polar ice, signal processing, estimation theory, and mesoscale atmospheric dynamics. He has over 250 publications in the open literature.

Dr. Long has received the NASA Certificate of Recognition several times. He is an Associate Editor for the IEEE Geoscience and Remote Sensing Letters.